Corrosion of 316L in Liquid Tellurium at 551°C

L. Martinelli, D. J. Young, S. Gossé, S. Bosonnet

Corrosion of 316L in Liquid Tellurium at 551°C

L. Martinelli[1], D. J. Young[2], S. Gossé[1], S. Bosonnet[1]

[1]CEA, DEN, Service de la Corrosion et du Comportement des Matériaux dans leur Environnement (SCCME), CEA, Université Paris-Saclay, F-91191, Gif-sur-Yvette, France,
[2]School of Materials Science & Engineering, University of New South Wales, Sydney, Australia

Abstract: Grade 316L stainless steel was exposed to liquid tellurium at 551^{o}C. Corrosion was rapid, leading to more than 100 μm loss of steel section in 30 min. The corrosion product was a mixed telluride scale, which thickened according to parabolic kinetics whilst simultaneously dissolving at its outer surface into the liquid tellurium. A mathematical model based on diffusion-controlled scale growth coupled with dissolution at a rate controlled by liquid phase diffusion is shown to describe scaling and dissolution kinetics successfully.

Keywords: Tellurium corrosion; telluride scale; dissolution; diffusion control

Introduction

Stainless steel grade 316L is often considered as fuel cladding in fast nuclear reactors, and its resistance to corrosion by fission products can of concern. Indeed, reaction between fission products and the cladding is the phenomenon limiting the life time of the cladding in the power plant. Among the many fission products released by the fuel, tellurium and cesium are considered as the most detrimental. These two elements are often considered to corrode jointly together with oxygen [1]-[3]. However before to carry out very complex experiment involving the presence of the 3 elements, corrosion of 316L by each of the three elements separately has been decided to be conduct. This study deals with the first step of this methodology, that is corrosion in pure Te.

Tellurium [4] melts at 450^{o}C, and can be liquid at operating temperatures at the cladding surface. Consequently, corrosion by liquid tellurium is considered in this study.

Corrosion by liquid tellurium also occurs in other nuclear concepts as in molten salts reactor in which tellurium is also a fission product and can be metallic in the salt. Feedback from Molten Salt Reactor Experiment (MSRE) indicate that Te is deposited under metallic form on metallic and graphite surfaces and can react with structural materials leading to Cr rich intergranular intermetallics formation Cr_3Te_4, Cr_3Te_6 that could lead to embrittlement [5]-[8].

Thus direct reaction between metal and Te(l) can be of practical concern.

The corrosion process is also of fundamental interest, as it involves formation of solid metal tellurides [4]-[13] and their dissolution into the melt.

This paper reports the results of a preliminary laboratory investigation of the kinetics of 316L corrosion in liquid tellurium, and the morphological evolution of the reaction products.

Thermodynamic considerations

The phase diagrams and thermodynamic interactions between the major alloying elements (Cr, Fe, Ni) and Te were studied by numerous authors: Cr-Te [14]-[16], Fe-Te [17]-[20] and Ni-Te [21] [22].

Thermodynamic information – metal solubilities in liquid Te, phases at equilibrium, standard Gibbs free energies of formation for the intermetallic tellurides – is of major importance when dealing with corrosion issues.

All these data made it possible to perform a thermodynamic assessment of these binary metal-chalcogen systems using the Calphad method [23] based on these thermodynamic and phase diagram data. These metal-tellurium binary and ternary systems are under development in order to obtain a thermodynamic database dedicated to fuel-cladding interaction applications [19][20].

From these thermodynamic modelling operations, the liquidus line of each binary system was calculated. In *Figure 1*, the metal solubility limits were calculated as a function of temperature inverse. At 823 K (10000/T=12.15 K^{-1}), liquid Te has solubility limits of 5.33 at. % for iron [20], 4.55 at. % for nickel and 2.54 at. % for chromium. From Calphad modelling, as shown in *Figure 1*, the solubility limit of iron, chromium and nickel in liquid Te is given by the following relations:

$$S^{Fe}_{Te(liq)}(at.fr.) = 429 - 23518/T - 150log_{10}(T) + 4.54\text{x}10^{-2}T$$

for 720<*T*(K)<919

$$S^{Fe}_{Te(liq)}(at.fr.) = 22 - 9.01log_{10}(T) + 5.32\text{x}10^{-3}T$$

for 919<*T*(K)<1039

$$S^{Fe}_{Te(liq)}(at.fr.) = 344 - 133log_{10}(T) + 5.60\text{x}10^{-2}T$$

for 1039<*T*(K)<1088

(1)

$$S^{Cr}_{Te(liq)}(at.fr.) = 4.38 - 1.82log_{10}(T) + 1.16\text{x}10^{-3}T,\ 753 < T(K) < 1276 \quad (2)$$

for 720<*T*(K)<1160

$$S^{Ni}_{Te}(at.fr.) = -1378 + \frac{62197}{T} + 508log_{10}(T) - 0.26T + 5.13\text{x}10^{-5}T^2 \quad (3)$$

These high solubilities highlight the possible extensive loss of steel depending on the amount of liquid tellurium, and the dissolution rate. The high temperature loops correspond to the congruent melting of the Te-rich binary intermetallics.

Figure 1: Binary Cr, Fe, Ni solubilities in liquid Te (at. fr.) as a function of inverse temperature (K^{-1})

Experimental

Corrosion tests were performed using 316L stainless steel (composition in *Table 1*) ground with SiC paper to a 1200 grit finish before the experiments. Samples of dimensions 30x10x0.5 mm, were immersed one by one in a crucible containing 107 g of liquid Te at 824 K. The volume of liquid Te was 18.8 cm^3 in a pyrex crucible of 5.3 cm diameter, producing a liquid height of 0.85 cm. A diagram of the facility is presented in *Figure 2*. A thermocouple immersed in the liquid near the sample provided a continuous reading of the temperature. As the thermal mass of the steel sample was very much less than the Te melt, temperature changes during sample insertion were minimal. Samples were fixed by a Mo wire to a pyrex sample holder and immersed in the liquid Te, above and approximately parallel to the bottom of the crucible. The crucible was contained in a glass reactor which was swept continuously with Argon 6.0 (99.9999 at% pure) to maintain an inert environment. The reactor was contained in a glove box to avoid contamination from the atmosphere. Considering the free energy of formation of telluride oxide all Fe, Cr or Ni oxides can be formed in liquid Te, literature [10]-[12] shows that Te reacts directly with steel elements (Fe, Cr, Ni) to form intermetallics. Consequently, oxygen impurities presence is not an issue in this liquid metal (unlike for other liquid alloys in nuclear systems as for instance lead alloys).

Figure 2: Schematic diagram of the facility (a) and enlargement of the sample holder (b).

Five samples were immersed, one after the other in the same melt, for various durations. In the event of a dissolution process, the liquid Te is expected to become continuously enriched in corrosion products. Thus the concentrations of Fe, Cr, Ni increase as a function of accumulated steel immersion time in the liquid. The corrosion rate is then expected to decrease as the liquid is enriching in dissolved Fe, Cr, Ni. For this reason, it could be considered that liquid metal should be renewed after each test. However, steel dissolution is very rapid. In order to study long term kinetics (longer than a few minutes) without completely destroying the steel specimen, it is necessary to slow the dissolution rate by using Te(l) which already contains solute metals, (Fe, Cr, Ni etc), in the proportions present in the steel. To conduct multiple series of exposures in liquids made up to different compositions corresponding to different degrees of 316L dissolution, would be an inefficient (and prohibitively expensive) approach. The most efficient manner to disentangle the effects of time and liquid composition on dissolution rate is the following experimental sequence:

enrichment of the liquid Te in solute metals, (Fe, Cr, Ni etc) is performed by dissolution of samples themselves as it will be seen that no preferential dissolution occurs, all elements dissolve evenly.

The first sample was immersed for 1 min and the second for 10 min, leading in the latter case to total dissolution of that sample. The third sample was immersed also for 10 min, the fourth 30 min and the fifth 5 min. The sequence of immersion experiments and their duration are shown in *Figure 3*. As previously explained, the purpose of this procedure was to examine the effect of liquid composition on corrosion rate.

Figure 3: Sequence of exposures, showing their duration and corresponding accumulated concentration of dissolved iron calculated from the loss of thickness of each sample.

Table 1: Chemical composition of 316L in wt%

Fe	Cr	Ni	Mo	Mn	Si	P	N	C	S
Bal.	16.82	10.17	2.08	1.84	0.64	0.026	0.025	0.016	0.003

Results

Successive steel specimens were immersed in and withdrawn from the same melt in the sequence shown in *Figure 3*. Apart from the second specimen, which had completely dissolved, all specimens emerged from the melt covered with a thin film of liquid. Cross-sections of the remaining steel together with the adhering solidified melt are shown in *Figure 4* and 5. Metal tellurides visible in the micrographs have two different origins. Those in the thin corrosion scale at the steel surface were developed in the corrosion process. This thin scale is seen at the steel surface with its outer boundary marked by an orange dotted line in *Figure 4* and 5. The much larger ones seen as precipitates in the frozen melt adhering to the scale were formed during cooling. The thin corrosion scale at the steel surface is analysed by SEM-EDX in Figure 8: it is composed of Fe, Cr, Ni, Te. Its composition seen from the *Figure 8* profile corresponds, on average, to metal telluride, MTe_2. Within the layer are discrete regions of chromium enrichment, indicating the presence of a multi-phase telluride mixture composed of different Cr- and Fe rich phases. Whilst the scale is continuous and apparently dense (*Figure 6* and *7*), individual phases are not.

Figure 4: Optical Microscope image of cross-sections of 316L showing adherent solidified liquid after immersion in melt for indicated times. (a) corresponds to exposure A in Fig 3; (b) to exposure E in Fig 3; (c) to exposure C in Fig 3; (d) to exposure D in Fig 3. Exposure times

noted on each micrograph. The corrosion scale boundary is marked by an orange dotted line. The precipitates in the solidified melt are Fe, Cr, Ni tellurides formed during cooling.

Figure 5: Optical Microscope image of cross-sections of 316L showing adherent solidified liquid after immersion in melt for exposure D in Fig 3 (30 minutes). The adherent corrosion scale is marked by an orange dotted line. The precipitates in the solidified Te melt are Fe, Cr, Ni tellurides formed during cooling.

Above the scale, melt solidification has led to precipitation from the parent melt of particles, the volume fraction of which increases with accumulated immersion time. As seen in Figure 4, the size of the individual precipitates is independent of immersion time and therefore of solute concentration. Compositional analysis of the various phases by EDX produced the qualitative maps of *Figure 6* and *Figure 8*, and the quantitative profiles of *Figure 7*.

The particles precipitated during solidification of the melt are iron or chromium tellurides, of approximate composition (Fe,Ni,Cr)Te_2. X-ray diffraction analysis of the solidified melt on a stainless steel specimen (shown in *Figure 9*) confirmed the presence of the phase $FeTe_2$. From the Calphad modelling (*Figure 10*, *Figure 11*), the calculated Te rich domain of the Cr-Fe-Te isothermal section at 823 K confirms the presence of a three phases domain where liquid Te equilibrates with two different intermetallics: Te_{liq} + Cr_3Te_4 + $FeTe_2$. In the present study the phase Cr_3Te_4 could not be detected, neither with EDX (*Figure 7*) nor with XRD (*Figure 9*).

Figure 6: SEM image (a) and EDX maps (b), (c) of corrosion products) and solidified liquid on 316L after immersion in the melt for 1 min (exposure A). The corrosion scale boundary is marked by an orange dotted line. The precipitates in the solidified melt are Fe, Cr, Ni tellurides formed during cooling.

Figure 7: EDX line scans across reaction zone and into solidified melt after 10 min immersion (Exposure C).

Figure 8: SEM image (a) and EDX maps (b), (c) of corrosion products and solidified liquid on 316L after immersion in the melt for 30 min (exposure D). The corrosion scale boundary is marked by an orange dotted line. The precipitates in the solidified melt are Fe, Cr, Ni tellurides formed during cooling.

Figure 9: X-Ray diffraction patterns obtained from the sample surface (covered by solidified melt) after 10 min (diffractogram (a) in blue) (exposure C) and 30 min (diffractogram (b) in grey) (exposure D) immersion. Identification of peaks, using ICDD cards (#00-014-0419; 00-

036-1452; 04-004-4697), confirms the presence of Te, $MoTe_2$ and $FeTe_2$. Presence of $MoTe_2$ is due to the use of Mo suspension wire for the samples.

Figure 10: Binary phase diagram of (a) Ni-Te calculated from [24], (b) Fe-Te calculated from [20], (c) Cr-Te [25]

Figure 11: Te rich domain of the Cr-Fe-Te isothermal section calculated at 823 K, extrapolation from the binary systems.

Figure 12: SEM-QBSD image of cross section of 316L after immersion in the melt for 30 min (Exposure D).

Figure 13: Scale growth kinetics. The red plain line corresponds to a parabolic kinetics and the blue dotted line corresponds to a linear kinetics.

No depletion profiles are evident in the steel beneath its corroded surface, indicating that no preferential reaction of any element occurred. This is confirmed by a comparison of steel and scale compositions: the former has an Fe/Ni ratio of 7.5 and an Fe/Cr ratio of 3.7, whilst the scale has corresponding ratios measured as 8.4 and 3.7 (see *Figure 7*).

The scale continues to thicken with time. As seen in *Figure 13*, a linear rate equation could be used to provide an empirical description of the data. However, it lacks physical meaning because it incorrectly implies a thick scale at time zero. More realistically scale growth kinetics can be described using parabolic kinetics.

$$X^2 = 2k_p t \tag{4}$$

where X is the scale thickness grown in time, t, and k_p the parabolic rate constant. It is noted that each point in *Figure 13* represents a different specimen, each inserted with a clean, bare surface into the melt. Consequently the specimen immersed for 5 minutes (Experiment E, *Figure 3*) is the second point of the graph: although the specimen was immersed for only 5 minutes, the liquid Te was extensively enriched in dissolved Fe as a result of previous experiments (*Figure 3*).

Overall corrosion of the steel was assessed by measuring the thickness of the remaining steel section and calculating section loss for each specimen after a single immersion. The kinetics of this process are seen in *Figure 14* to be neither linear nor parabolic. It is also clear that the rate of steel consumption is far higher than the rate of scale growth, consistent with the appearance of increasing amounts of Fe, Cr, Ni and Mo in the melt, as evidenced by the growing volume fraction of MTe_2 precipitates in the solidified liquid (*Figure 6*, *Figure 8*, *Figure 12*).

Figure 14: Steel corrosion kinetics. The blue plain line corresponds to a parabolic kinetics and the blue dotted line corresponds to a linear kinetics.

The amount of metal dissolved into the melt as steel is consumed is readily calculated from simple mass balance, using the measured loss of steel thickness. The resulting average

concentrations are then found by taking into account the relative volumes of melt and steel consumed according to the following relation:

$$\bar{C}_{Fe(mol\,cm^{-3})} = 2\frac{\mu_{Te}}{M_{Fe}m_{Te}}\,SX_{316}\mu_{316}\,W_{316}^{Fe} \qquad (5)$$

Here $\bar{C}_{Fe(mol\,cm^{-3})}$ is the average dissolved iron concentration in the liquid Te, μ_{316L} and μ_{Te} are respectively the density of solid iron and liquid tellurium (g cm^{-3}), M_{Fe} is the molar mass of Fe (g mol^{-1}), m_{Te} is the mass of Te in the crucible (g), S is the sample surface area (cm^2), X_{316} is the loss of thickness of 316L of one face of the sample (cm), and W_{316}^{Fe} is the weight fraction of iron in 316. Edge effects have been ignored.

Increments in dissolved iron concentration can be calculated in this way from the specimen consumption observed in each single exposure experiment. In the first such exposure, the initial solute iron concentration was zero, and the calculated increment is therefore equal to the final concentration. In subsequent exposures, of course, it is not. For this reason, and because of the unusual sequence of exposures (see *Figure 3*), the results are shown in the bar chart of *Figure 15* as concentration increments for the succession of corrosion processes specified in *Figure 3*.

Figure 15: Iron dissolution kinetics for exposures A to E (defined in Figure 3) as calculated from mass balance, and predicted from interface reaction model (Equation 11) and from diffusion model (Equation 12).

Discussion

Corrosion of 316L in Te(l) produces a thin surface layer of metal tellurides and extensive dissolution into the melt. During this process, the telluride-steel interface remains flat over the period observed (*Figure 12*). On this basis, it is concluded that liquid metal is not present at the steel surface, and that dissolution takes place only at the outer surface of the telluride layer. If, conversely, the melt penetrated a porous telluride layer, the rapid dissolution of steel at penetration locations would lead to an irregular steel-telluride interface, an outcome not arrived at under the reaction conditions employed.

A solid reaction product layer develops on the steel surface, and thickens with time (*Figure 4* to *Figure 7*, *Figure 13*). To investigate whether this is a steady-state situation, it is desirable to map the locus of composition observed across the steel – telluride layer system onto the appropriate phase diagram for the reaction system, to see if it is consistent with local equilibrium.

Unfortunately, no ternary phase diagrams are available and the thermodynamic data is limited in the Fe-Ni-Te ternary system. In the binaries, both Fe and Ni form the nonstoichiometric phases $FeTe_2$ and $NiTe_2$ at 823 K. The situation for the Cr-Te system is more complex, with a series of tellurides thought to be stable at 823 K, with the highest being Cr_3Te_4. As Ni is a minority element in both the steel and in the analysed telluride reaction product layer (*Figure 7*), it is ignored here, and the chemical system is approximated as Cr-Fe-Te.

The isothermal section shown in *Figure 11* has been constructed on the basis of the binary diagrams. For simplicity, the Te rich side of the Cr-Te system is approximated as forming a single intermetallic Cr_3Te_4 phase. The reciprocal Fe and Cr solubilities in Cr_3Te_4 and $FeTe_2$ are unknown and not considered in the phase diagram. Nevertheless, due to the different structures of these intermetallics (Cr_3S_4 for Cr_3Te_4 [16] and FeS_2 pyrite prototype for $FeTe_2$ [17]), small reciprocal Cr and Fe solubilities may exist, but full intersolubility is regarded as unlikely.

The locus of composition in the solid part of the reacting system taken from the profiles in *Figure 7* is mapped onto the approximate Fe-Cr-Te ternary diagram of *Figure 11*. It is seen to be consistent with local equilibrium, corresponding to a diffusion path. In the development which follows, mass transport in the solid telluride layer is taken to be diffusion controlled. The processes of telluride dissolution into the melt and transport of solute away from the telluride-melt interface, which represent the major part of the corrosion reaction are considered first.

Dissolution Reaction

The telluride product layer is closely similar in Fe-Ni-Cr content to the substrate steel. Thus the Fe/Ni ratio in the layer is found to be 8.4 compared with 7.5 in the steel, and the Fe/Cr ratio is 3.7 in both (see *Figure 7*). Since, moreover, little depletion is apparent in the subsurface alloy, it is concluded that the proportions of Fe, Ni and Cr solutes in the melt are the same as in the steel. Dissolution of the majority component, Fe, is considered and the flux of iron across the solid-liquid interface, $J_{Fe}^{s/l}$, is evaluated.

In the simplest case, the iron content of the melt has no influence on dissolution rate, and

$$J_{Fe}^{s/l} = k \tag{6}$$

with k a constant. Then if mass transfer within the liquid phase is rapid in comparison to the dissolution rate

$$\bar{C}_{Fe} = \bar{C}_{Fe}^{0} + kt \tag{7}$$

with $\bar{C}_{Fe}$ the average concentration of Fe in the melt, and $\bar{C}_{Fe}^{0}$ its original value. The prediction of linear kinetics for iron dissolution is clearly incorrect (*Figure 14*), and a more realistic description is sought.

Assuming now that the driving force for iron dissolution is the difference between solute iron activity, a_{Fe}, and its value at equilibrium, $a_{Fe}^{(eq)}$, then

$$J_{Fe}^{s/l} = k_r\left(a_{Fe}^{eq} - a_{Fe}\right) \tag{8}$$

with k_r the rate constant for the phase boundary mass transfer process. If it is also assumed that transport within the melt is rapid, and the value of a_{Fe} is essentially uniform in the melt, then Eqn (8) yields

$$\frac{d\bar{C}_{Fe}}{dt} = \gamma_{Fe} k_r G \, (C_{Fe}^{eq} - \bar{C}_{Fe}) \quad (9)$$

where γ_{Fe} is the activity coefficient for Fe in the melt, C_{Fe}^{eq} the iron concentration at equilibrium in liquid Te (assumed equal to iron solubility limit given in Eqn (4): 2.5x10^{-3} mol/cm^{-3}) and *G* a geometric factor relating the surface area of the specimen to the volume of liquid:

$$G = \frac{S}{\pi R^2 X_{Te}}$$

Here *S* is the sample surface area (cm^2), *R* is the crucible radius (cm) (equal to 2.65 cm) diameter and X_{Te} is the depth (cm) of liquid Te in the crucible (equal to 0.85 cm).

Integration of Eqn (9) using the initial condition

$$\bar{C}_{Fe} = \bar{C}_{Fe}^0 \text{ at } t_0 \quad (10)$$

leads to the result

$$\frac{(C_{Fe}^{eq} - \bar{C}_{Fe})}{(C_{Fe}^{eq} - \bar{C}_{Fe}^0)} = e^{-\beta(t-t_0)} \quad (11)$$

where $\beta = \gamma_{Fe} k_r G$.

This equation for interfacial reaction controlled dissolution can be tested by applying it to each of the successive stages of the experiment charted in *Figure 3*, using the indicated, successively higher values of $\bar{C}_{Fe}^0$ as initial values in calculating incremental increases in dissolved iron concentration. The value of $\beta = 9x10^{-4}$ s^{-1} was arrived at in optimising the fit of Eqn (11) to experimental data. Concentrations calculated in this way are compared with those found from simple mass balance in *Figure 15*. It is seen that the interface reaction rate control model of Eqn (11) provides a qualitatively reasonable description. In particular, it successfully predicts the complete dissolution of the steel in experiment B, the first 10 min exposure. In addition, it succeeds in predicting that less dissolution occurs in the second of the two 10 min experiments, B and C, a consequence of the higher value of $\bar{C}_{Fe}^0$present in experiment C. However, it significantly underestimates the rate of dissolution for exposures A and E (*Figure 3*, *Figure 15*). It is evident that mass transfer within the liquid slows dissolution rates, and this process must be incorporated into the description.

Diffusion Model

Assuming now that the controlling factor for iron dissolution is the diffusion of iron in the finite volume of liquid Te, and that the rate of dissolution is much more rapid, the concentration of dissolved iron is constant at the solid/liquid interface and equals C_{Fe}^{eq}. If edge effects are ignored and convection in the isothermal melt pool can also be neglected, the situation can be modelled as shown in *Figure 16*.

Figure 16: Diagram of the diffusion model for solute entering the melt.

If the steel specimen is located symmetrically within the melt, then uptake of iron by the two halves of the Te(l) reservoir can be modelled as sorption of a solute by a sheet of finite thickness, X_{Te}, with surfaces at a constant concentration, C_{Fe}^{eq}. The average concentration of iron, $\bar{C}_{Fe}$, within the liquid increases as a function of time according to the following equation given by Crank [26]:

$$\frac{(\bar{C}_{Fe}-\bar{C}_{Fe}^{0})}{(C_{Fe}^{eq}-\bar{C}_{Fe}^{0})} = 1 - \sum_{n=0}^{\infty} \frac{8}{(2n+1)^2\pi^2} e^{-\frac{(2n+1)^2\pi^2 D(t-t_0)}{X_{Te}^2}} \qquad (12)$$

where D is the diffusion coefficient (cm^2 s^{-1}) of dissolved iron in the liquid tellurium and X_{Te} is the depth (cm) of liquid Te in the crucible (equal to 0.85 cm). The value of C_{Fe}^{eq} is set at the solubility limit at this temperature, 2.5x10^{-3} mol/cm^{-3}.

Just as for Eqn (11), Eqn (12) for diffusion controlled dissolution can be tested by applying it to each of the successive stages of the experiment charted in *Figure 3*, using the indicated, successively higher values of $\bar{C}_{Fe}^{0}$ as initial values in calculating incremental increases in dissolved iron concentration. Concentration increments calculated in this way are compared with those found from simple mass balance in the bar chart of *Figure 15*. The only unknown value of Eqn (12) is the diffusion coefficient of Fe in liquid Te. This diffusion coefficient is adjusted to reach the best fit for Eqn (12) with the experimental data for dissolved iron concentration. The best fit is obtained for a diffusion coefficient equal to 4x 10^{-5} cm^2 s^{-1}, which agrees with the usual values of diffusion coefficients in liquids. It seems therefore that the neglect of convection was justified in this case. Moreover, it is seen in *Figure 15* that the volume mass transfer rate control model of Eqn (12) provides a relatively improved description of the iron dissolution kinetics.

On this basis, it is concluded that the rate controlling step for the dissolution process is the diffusion of dissolved Fe in the Te melt. In addition, a description of the thickening kinetics of the adherent layer, or scale, is required.

Growth of the scale

The scale is simultaneously growing at the expense of the underlying steel, and dissolving at its outer surface. The dissolution part could, in principle, be either reaction rate controlled (Eqn 11) or diffusion rate controlled (Eqn 12). Considering these two dissolution mechanisms, the growth of the adherent layer becomes Eqn (13) for parabolic scale growth coupled with an interface reaction dissolution process, and Eqn (14) for parabolic scale growth coupled with a diffusion controlled dissolution process:

$$\frac{dX_{FeTe2}}{dt} = \frac{k_p^{MTe2}}{X_{FeTe2}} - \frac{X_{Te}}{2C_{Fe}^{FeTe2}}\beta\left(C_{Fe}^{eq} - \bar{C}_{Fe}^{0}\right)e^{-\beta(t-t_0)} \qquad (13)$$

$$\frac{dX_{FeTe2}}{dt} = \frac{k_p^{MTe2}}{X_{FeTe2}} - \frac{4D\left(C_{Fe}^{eq} - \bar{C}_{Fe}^{0}\right)}{C_{Fe}^{FeTe2} X_{Te}} \sum_{n=0}^{\infty} e^{-\frac{(2n+1)^2 \pi^2 D(t-t_0)}{X_{Te}^2}} \quad (14)$$

Here X_{FeTe2} is the thickness of the corrosion layer, D is the diffusion coefficient of dissolved iron in the liquid tellurium and X_{Te} is the depth of liquid Te in the crucible, C_{Fe}^{FeTe2} is the concentration of Fe in the corrosion layer, approximated as $FeTe_2$ and β the apparent dissolution constant as defined in Eqn (11).

In order to fit Eqn (14) to experimental results, a simplified equation is used, considering only the first term in the summation (only n=0). This simplification underestimates the dissolution part and leads to:

$$\frac{dX_{FeTe2}}{dt} = \frac{k_p^{MTe2}}{X_{FeTe2}} - \frac{4D\left(C_{Fe}^{eq} - \bar{C}_{Fe}^{0}\right)}{C_{Fe}^{FeTe2} X_{Te}} e^{-\frac{\pi^2 D(t-t_0)}{X_{Te}^2}} \quad (15)$$

Eqn (13) and (15) are numerically solved using Mathematica software. Assuming an apparent dissolution constant β equal to $9x10^{-4}$ s^{-1} and a diffusion coefficient D equal to 4x 10^{-5} cm^2 s^{-1} (as obtained fitting respectively Eqn (11) and (12) on experimental data of *Figure 15*), the best fits for Eqn (13) and Eqn (15) on experimental scale thickness are given in *Figure 17* together with experimental data.

The fits are seen to be reasonably good, with the exception of the 5 min exposure. Optimisation of the fit leads to k_p=5 x 10^{-9} cm^2s^{-1} for diffusion model (Eqn (15)) and to k_p=6.7 x 10^{-9} cm^2s^{-1} for interface reaction model (Eqn (13)). These values of k_p can be compared to experimental results obtained in Te vapour by Lobb and Robins [11] and by Magara *et al* [27]. In their case, as the Te was gaseous, there was no dissolution of the corrosion product telluride layer. For Lobb and Robins, at 550°C, for 2.6 minutes and 7 hours of corrosion they obtained, respectively, an 11 and 17 µm thick scale. It can firstly be noted that this pair of values does not correspond to parabolic growth. However, using the k_p values (5-6.7 x 10^{-9} cm^2s^{-1} obtained by fitting Eqn (15)-(13)) to the present experimental data, the scale thicknesses are calculated to be equal to 12-14 µm and 159-183 µm for, respectively, 2.6 minutes and 7 hours of corrosion. The scale thicknesses obtained for 2.6 minutes of corrosion using the k_p of this study and the one measured directly by Lobb and Robins [11] in Te vapour are very close, providing further support for the proposed model of Eqn (15). However, the approximation to Eqn (14) leading to Eqn (15) is valid only at small values of *t*, and Eqn (15) fails at long times.

In Magara's work, at 650°C [27], an Fe-11.5Cr steel in contact with gaseous Te formed a parabolic growing telluride layer assumed to be $(Cr,Fe)_2Te_3$ (on the basis of unreliable EPMA analyses) and for which k_p was evaluated as 10^{-7} g^2 $cm^{-4}s^{-1}$. Adjusting for the fact that the corrosion scale is $FeTe_2$, the k_p value becomes 2.4 x 10^{-9} cm^2s^{-1}, which is very close to the values obtained in this study. The limiting step for this layer growth was deduced, from the parabolic constant activation energy and from Fe diffusion measurement in various iron tellurides [27]-[29], to be grain boundary diffusion of iron in δ'-iron telluride (δ'-$Fe_{0.66}Te$). In

the present study, the analysed scale phase is more probably ε-$Fe_{0.95}Te_2$, for which no Fe diffusion coefficient is available.

Figure 17: Scale growth kinetics: measured from SEM observation, (♦), and predicted from Equation 13 (❑) and Equation 15 (▨).

Figure 17 shows that the models (Eqn (13) and (15)) describe the experimental results relatively well, except for the thickness value after 5 min of immersion (experiment E, *Figure 3*), which is overestimated. Indeed, there is an important amount of dissolved Fe in the melt, as a result of the preceding experiments, and this limits the scale dissolution. For scale growth (which does not depend on the dissolved iron level), the rate is high as it corresponds to an early stage of reaction, when the scale thickness is small.

It is noted that both Eqn (13) and (15) are subject to error in evaluation, as they each calculate a small difference between two large terms (scale growth and scale dissolution). An additional complication is that the solute concentration in the melt is not directly measured: it is deduced from the observed steel section loss in a calculation which neglects scale formation.

The overprediction of scale thickness from Eqns (13) or (15) for the 5 min specimen corresponds to the underprediction of dissolution in this case (*Figure 17*, second point, and *Figure 15*, last exposure). Both models (Eqn (13) and (15)) fail for this one point, but remain reasonable overall for the dataset.

The proposed values of D, k_p and β given in this study are only order of magnitude estimates and should not be considered as reliable data a.

It is concluded on the basis of *Figure 15* and *Figure 17*, that the dissolution rate is likely controlled by diffusion of dissolved Fe in the liquid Te melt, and the growth of the adherent telluride layer is controlled by the competition between its parabolic thickening and its dissolution, the latter process being supported by metal diffusion in the melt.

Conclusions

Using the Calphad method, a thermodynamic approach is used to study the interaction between Stainless steel 316L and liquid tellurium. The developed thermodynamic database makes it possible to calculate the solubilities of the major alloying elements (Cr-Fe-Ni) in liquid Te. However, in this preliminary work, the calculated value for iron seems to be underestimated. The metal tellurides formed at 823 K by interaction with liquid Te are predicted to be Cr_3Te_4 and $FeTe_2$ Corrosion tests have now been carried out, and the observed intermetallics in the corrosion layers are MTe_2 type which is partly in accord with thermodynamic predictions.

From the kinetic point of view, steel consumption is faster than scale growth, indicating that simultaneous formation and dissolution of tellurides into the melt occurs.

A mathematical model based on simultaneous scale thickening according to parabolic kinetics and scale dissolution controlled by liquid phase diffusion describes reasonably well both scaling kinetics and solute accumulation in the melt.

In order to reinforce this model, more study is required: (i) further investigation should be undertaken for thermodynamics data acquisition in the quaternary system Fe-Ni-Cr-Te, in particular to determine the effects of Ni on telluride stabilities; (ii) corrosion experiments should be carried out in liquid Te flowing at controlled rates in order to discriminate between the interface reaction and diffusion controlled mechanisms. Finally, in this study, only Fe loss has been modelled, whereas the global 316L corrosion process has to be considered.

[1] Götzmann, O., A thermodynamic model for the attack behaviour in stainless steel clad oxide fuel pins. Journal of Nuclear Materials, 1979. 84(1-2): p. 39-54.
[2] Adamson, M. and E.A. Aitken, Chemical thermodynamics of Cs and Te fission product interaction in irradiated LMFBR mixed oxide fuels pins. Journal of Nuclear Materials, 1985. 130: p. 375-392
[3] Bradbury, M.H., S. Pickering, and W.H. Whitlow, A proposed mechanism for internal cladding corrosion in LMFBR mixed oxide fuel pins. Journal of Nuclear Materials, 1978. 78(2): p. 272-280.
[4] W. Batey, K. Q. Bagley, Journal of the British Nuclear Energy Society, 13 (1974), 49-61
[5] McCoy H.E. Jr., Status of materials development for molten salt reactors, (1978), ORNL-TM-5920
[6] Keiser J.R., Status of tellurium-Hastelloy N studies in molten fluoride salts, 1-23, oct (1977), ORNL/TM-6002
[7] Rosenthal M.W., Briggs R.B., Haubenreich P.N., Molten-salt reactor program - Semiannual progress report for perod ending August 31, 1972, mar (1973), ORNL-4832
[8] Rosenthal M.W., Haubenreich P.N., Briggs R.B., Molten-salt reactor program – The development status of molten-salt breeder reactors, aug (1972), ORNL-4812
[9] Y. Jia, H. Cheng, J. Qiu, F. Han, Y. Zou, Z. Li, X. Zhou, H. Xu, Journal of Nuclear Materials, 441, N 1–3, (2013), 372-379
[10] R.J. Pulham, M.W. Richards, Journal of Nuclear Materials, 171 (1990), 319-326
[11] R.C. Lobb, I.H. Robins, Journal of Nuclear Materials 62 (1976) 50-62
[12] T. Yutani, S. Nomura, S. Koyama, Y. Kuwajima, S. Ukai, Journal of Nuclear Materials, 201 (1993), 35-45
[13] T. Yutani, S. Nomura, S. Koyama, Y. Kuwajima, S. Ukai, Journal of Nuclear Materials, 201 (1993) 35
[14] H. Ipser, K.O. Klepp, K.L. Komarek, Monatshefte für Chemie, 111 N 3 (1980) 761-770
[15] R. Prasad, V. S. Iyer, Z. Singh, V. Venugopal, S. Mohapatra, D. D. Sood, The Journal of Chemical Thermodynamics, 20 (1988) 319-322
[16] H. Ipser, K. L. Komarek, K.O. Klepp, Journal of the Less-Common Metals, 92 (1983) 265-282
[17] H. Ipser, N. L. Komarek, H. Mikler, Monatshefte für Chemie, 105 (1974) 1322-1334
[18] H. Ipser, K. L. Komarek, Monatshefte für Chemie, 105 (1974) 1344-1361
[19] C.-M. Arvhult, S. Poissonnet; D. Menut, S. Gossé, C. Guéneau, Journal of Alloys and Compounds, 773 (2019) 314-326
[20] C.-M. Arvhult, C. Guéneau, S. Gossé, M. Selleby, Journal of Alloys and Compounds, 767 (2018) 883-893
[21] M. Ettenberg, K. L. Komarek, E. Miller, Journal of Solid State Chemistry, 1 (1970) 583-592
[22] K. O. Klepp, K. L. Komarek, Monatshefte für Chemie, 103 (1972) 934-946
[23] H. Lukas, S. G. Fries, B. Sundman, Cambridge University Press, Cambridge UK (2007)

[24] CM. Arvhult, C. Guéneau, S. Gossé, M. Selleby, submitted to Journal of Nuclear Materials
[25] G. Chattopadhyay, Journal of Phase Equilibria, 15, N 4 (1994)
[26] J. Crank, The mathematics of diffusion, p 48, Clarendon press, Oxford 1975
[27] M. Magara, T. Tsuji, K. Naito, Journal of Nuclear Science and Technology, 28 (1991) 721
[28] M. Magara, T. Tsuji, K. Naito, Journal of Nuclear Materials, 203 (1993) 179
[29] M. Magara, T. Tsuji, K. Naito, Journal of Nuclear Materials, 203 (1993) 172

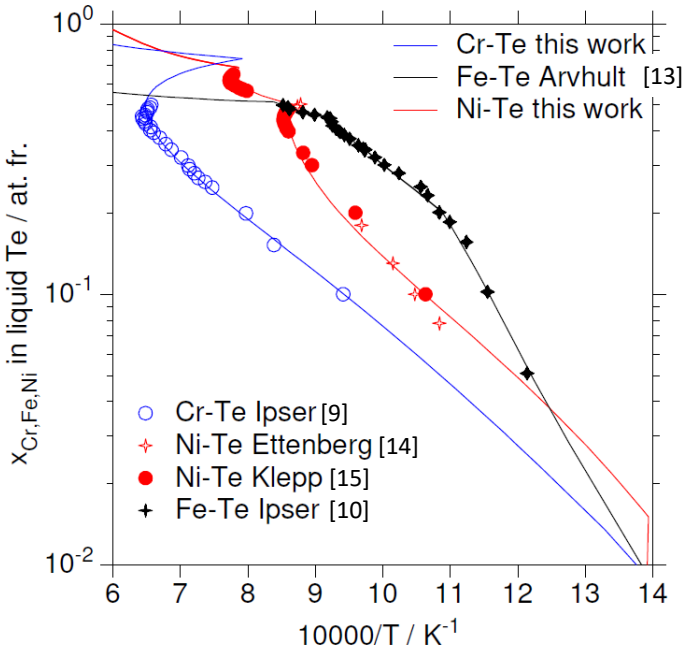

Figure 18: Binary Cr, Fe, Ni solubilities in liquid Te (at. fr.) as a function of inverse temperature (K^{-1}).

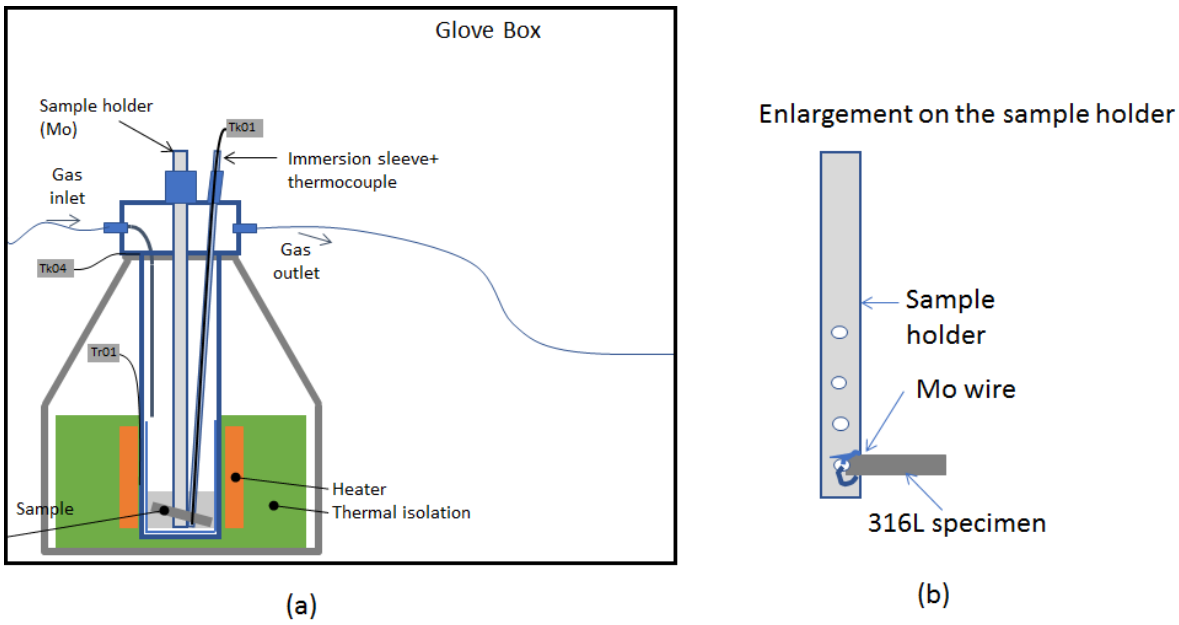

Figure 19: Schematic diagram of the facility (a) and enlargement of the sample holder (b).

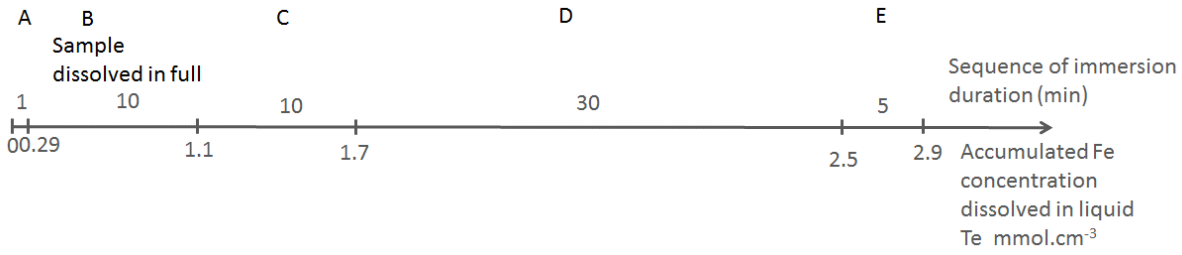

Figure 20: Sequence of exposures, showing their duration and corresponding accumulated concentration of dissolved iron calculated from the loss of thickness of each sample.

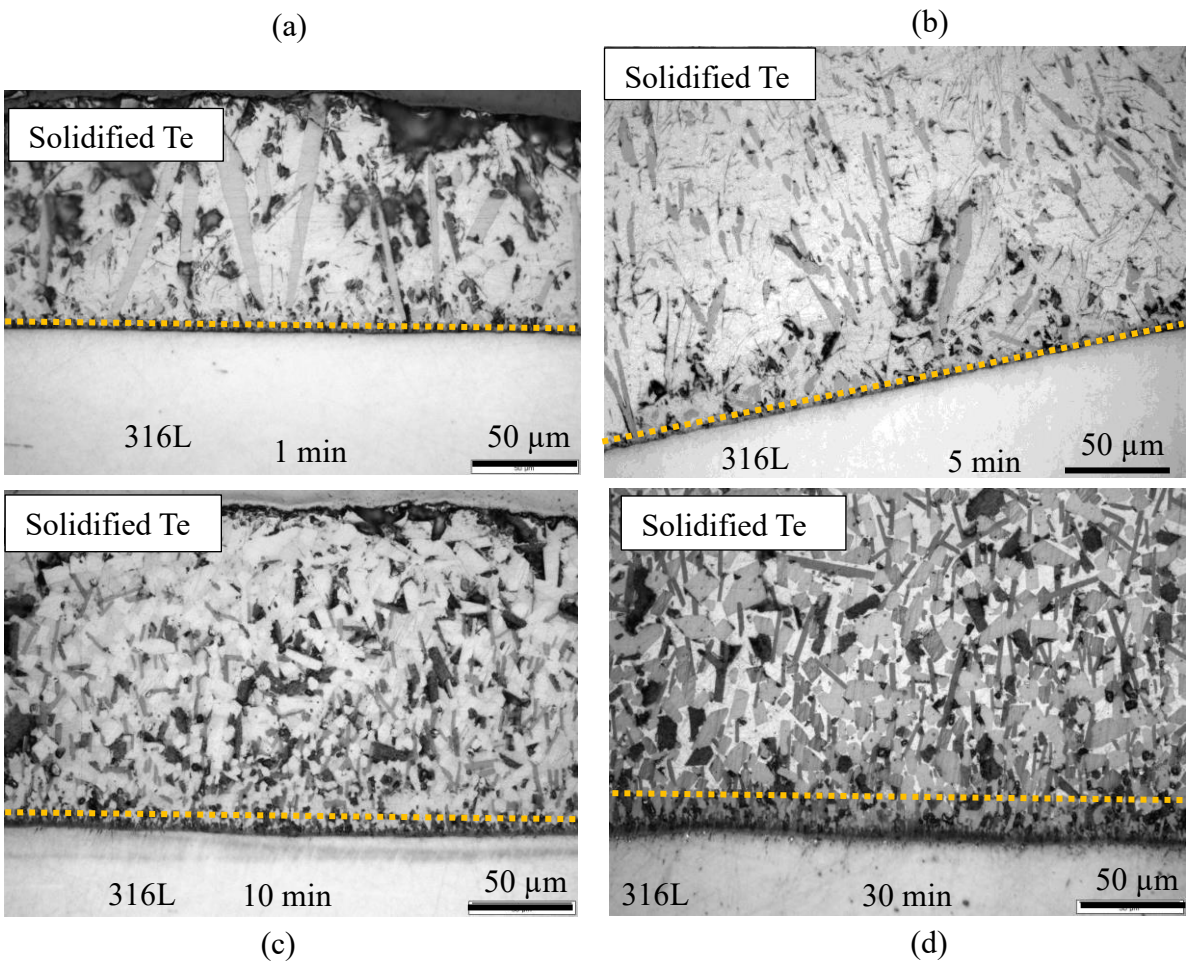

Figure 21: Optical Microscope image of cross-sections of 316L showing adherent solidified liquid after immersion in melt for indicated times. (a) corresponds to exposure A in Fig 3; (b) to exposure E in Fig 3; (c) to exposure C in Fig 3; (d) to exposure D in Fig 3. Exposure times noted on each micrograph. The corrosion scale boundary is marked by an orange dotted line. The precipitates in the solidified melt are Fe, Cr, Ni tellurides formed during cooling.

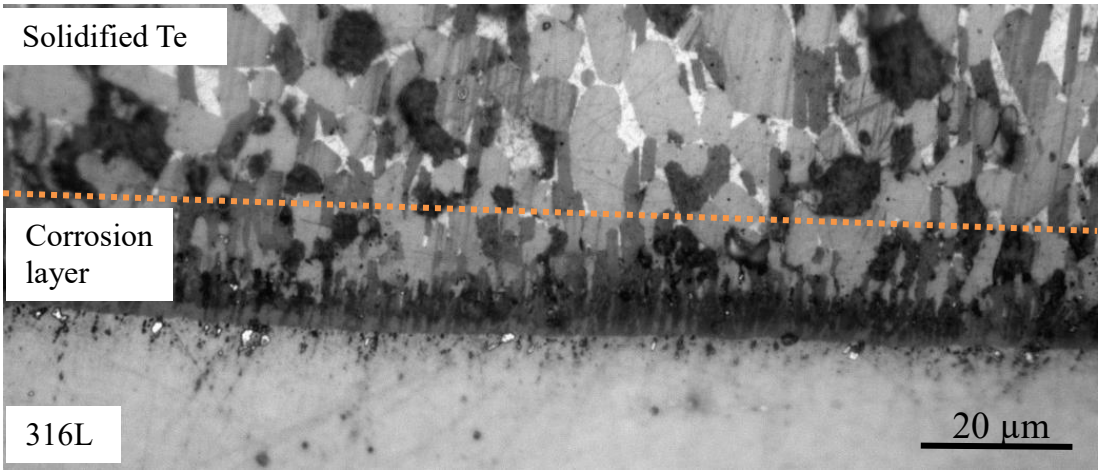

Figure 22: Optical Microscope image of cross-sections of 316L showing adherent solidified liquid after immersion in melt for exposure D in Fig 3 (30 minutes). The adherent corrosion scale is marked by an orange dotted line. The precipitates in the solidified Te melt are Fe, Cr, Ni tellurides formed during cooling.

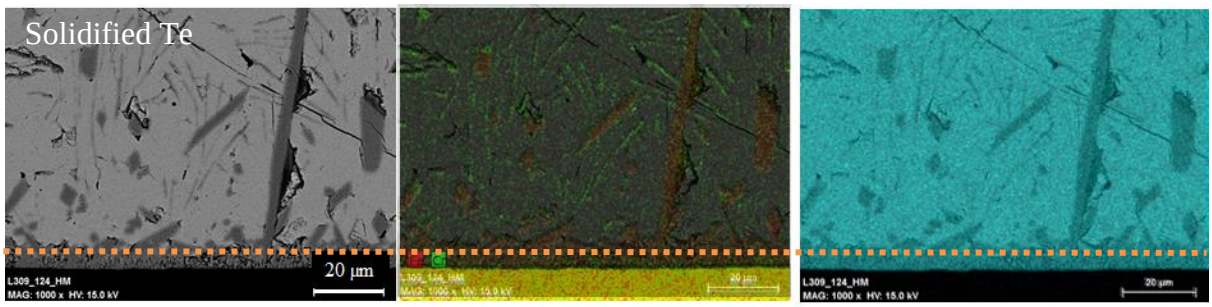

(a) QBSD image (b) Fe and Cr map (c) Te map

Figure 23: SEM image (a) and EDX maps (b), (c) of corrosion products) and solidified liquid on 316L after immersion in the melt for 1 min (exposure A). The corrosion scale boundary is marked by an orange dotted line. The precipitates in the solidified melt are Fe, Cr, Ni tellurides formed during cooling.

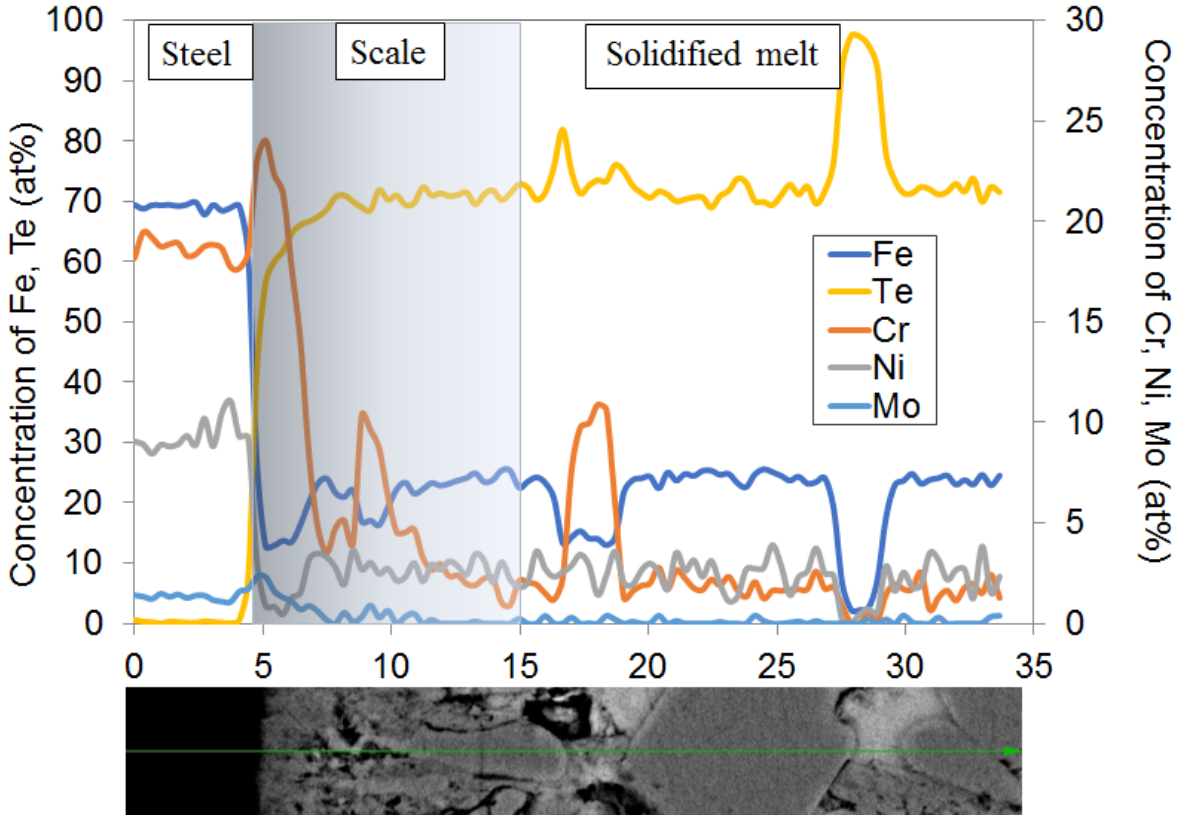

Figure 24: EDX line scans across reaction zone and into solidified melt after 10 min immersion (Exposure C).

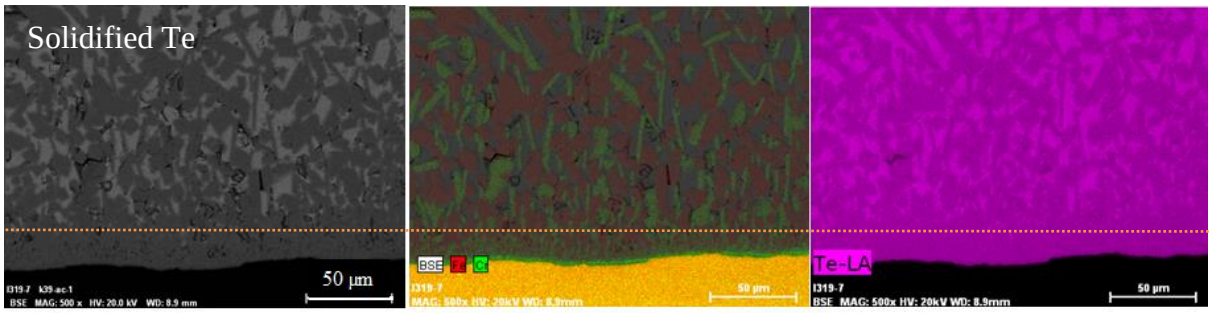

(a) QBSD image (b) Fe and Cr map (c) Te map

Figure 25: SEM image (a) and EDX maps (b), (c) of corrosion products and solidified liquid on 316L after immersion in the melt for 30 min (exposure D). The corrosion scale boundary is marked by an orange dotted line. The precipitates in the solidified melt are Fe, Cr, Ni tellurides formed during cooling.

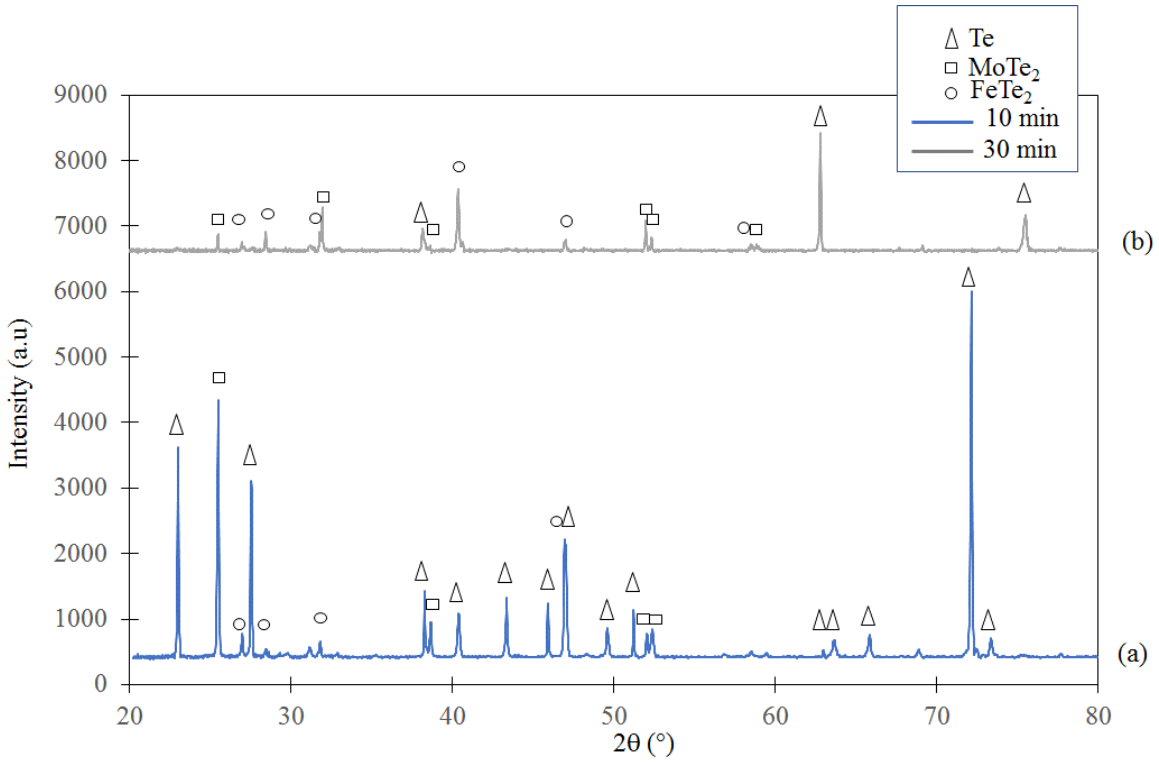

Figure 26: X-Ray diffraction patterns obtained from the sample surface (covered by solidified melt) after 10 min (diffractogram (a) in blue) (exposure C) and 30 min (diffractogram (b) in grey) (exposure D) immersion. Identification of peaks, using ICDD cards (#00-014-0419; 00-036-1452; 04-004-4697), confirms the presence of Te, $MoTe_2$ and $FeTe_2$. Presence of $MoTe_2$ is due to the use of Mo suspension wire for the samples.

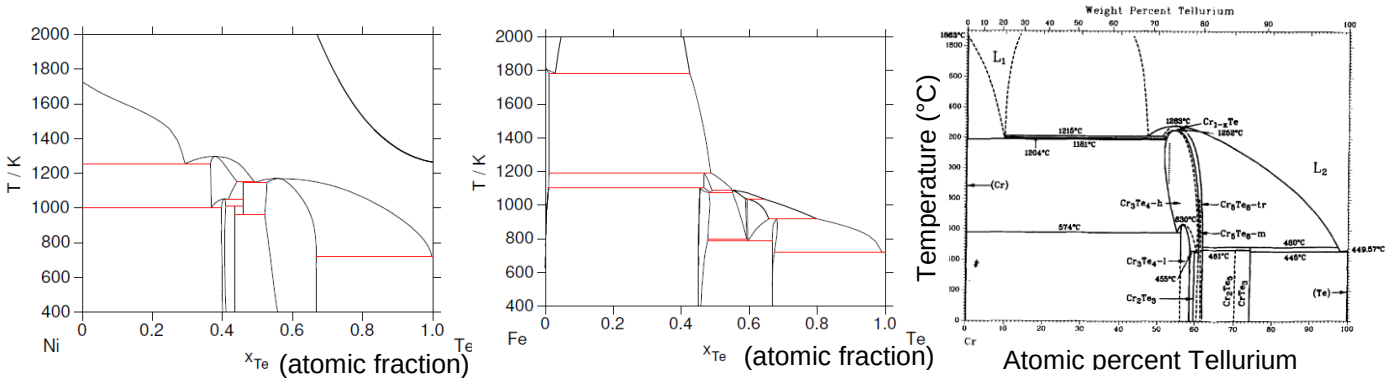

(a) Ni-Te (b) Fe-Te (c) Cr-Te

Figure 27: Binary phase diagram of (a) Ni-Te calculated from [24], (b) Fe-Te calculated from [20], (c) Cr-Te [25]

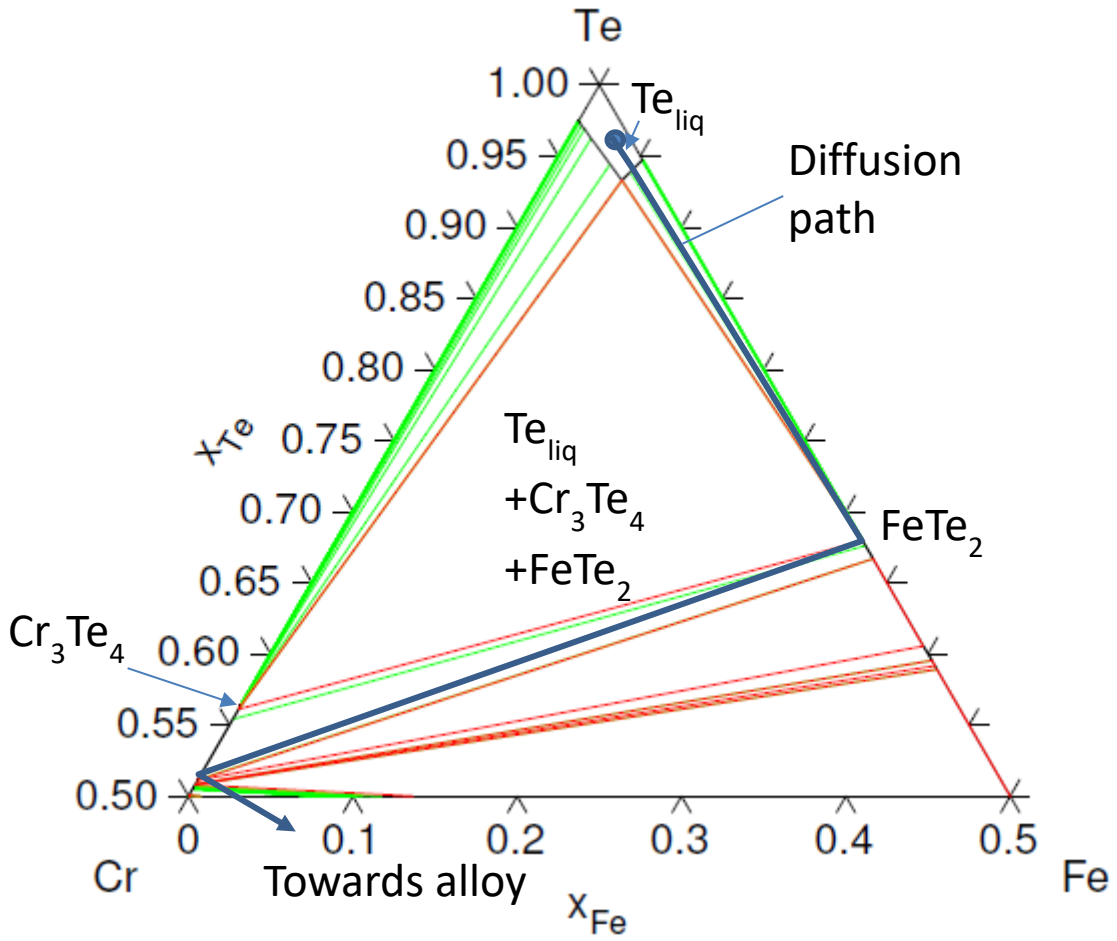

Figure 28: Te rich domain of the Cr-Fe-Te isothermal section calculated at 823 K, extrapolation from the binary systems.

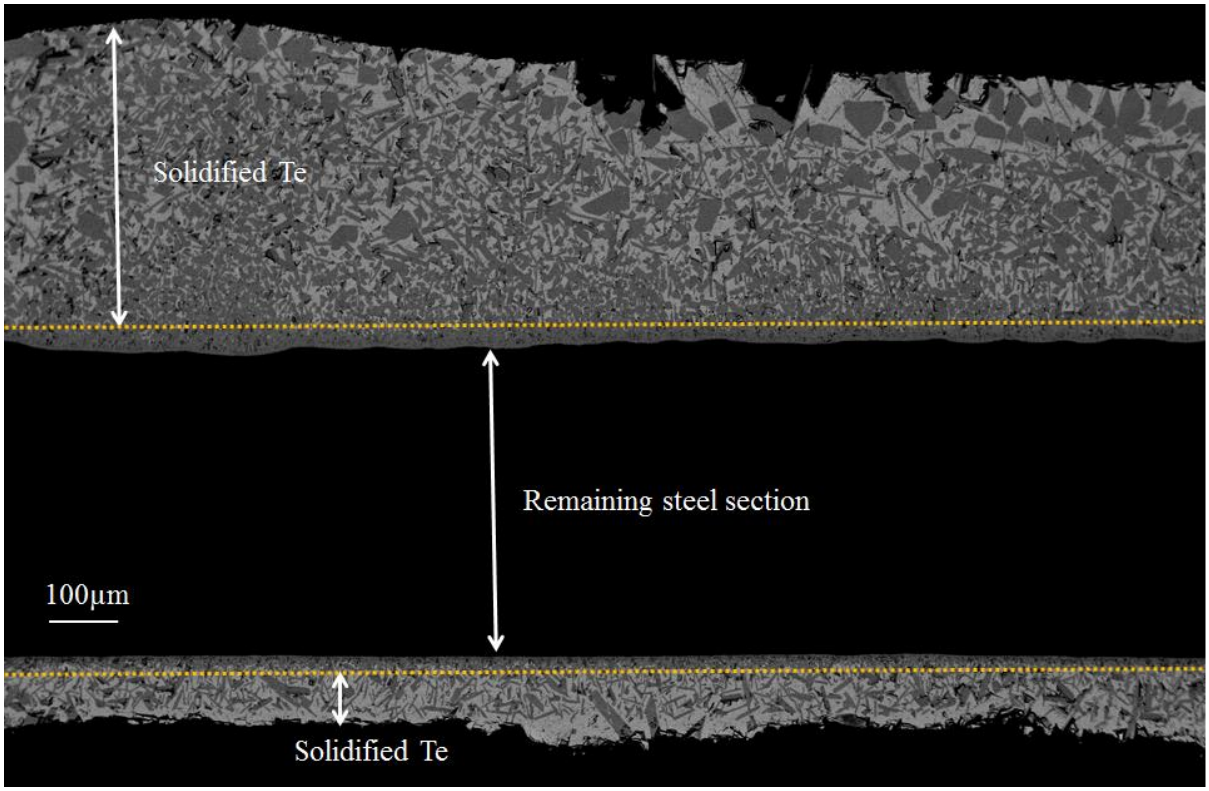

Figure 29: SEM-QBSD image of cross section of 316L after immersion in the melt for 30 min (Exposure D). The corrosion scales boundaries are marked by an orange dotted line. The precipitates in the solidified melt are Fe, Cr, Ni tellurides formed during cooling.

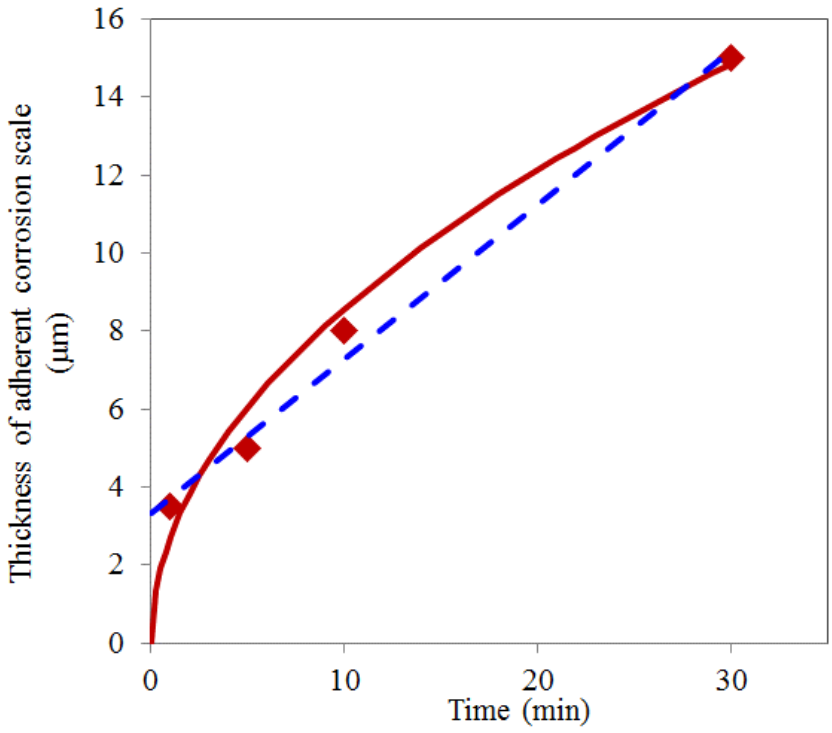

Figure 30: Scale growth kinetics. The red plain line corresponds to a parabolic kinetics and the blue dotted line corresponds to a linear kinetics.

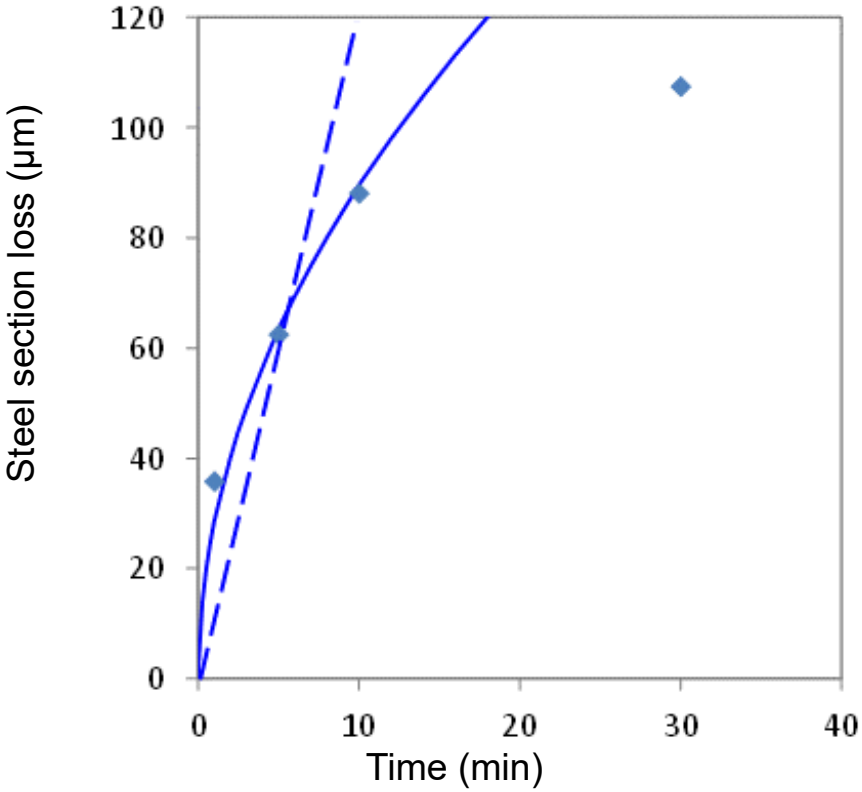

Figure 31: Steel corrosion kinetics. The blue plain line corresponds to a parabolic kinetics and the blue dotted line corresponds to a linear kinetics.

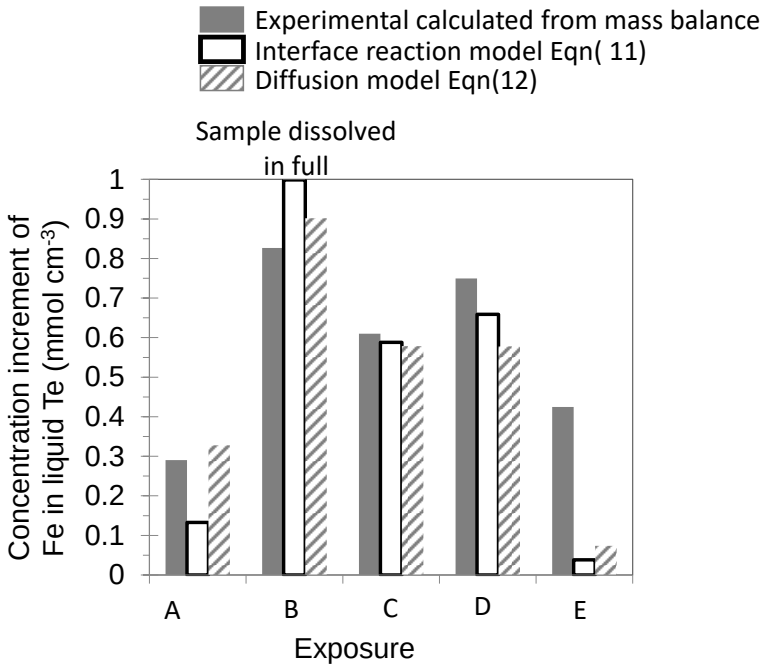

Figure 32: Iron dissolution kinetics for exposures A to E (defined in Fig 2) as calculated from mass balance, and predicted from interface reaction model (Equation 11) and from diffusion model (Equation 12).

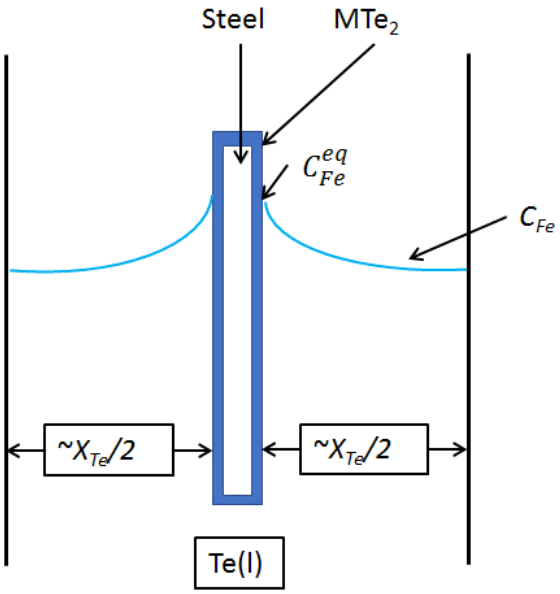

Figure 33: Diagram of the diffusion model for solute entering the melt.

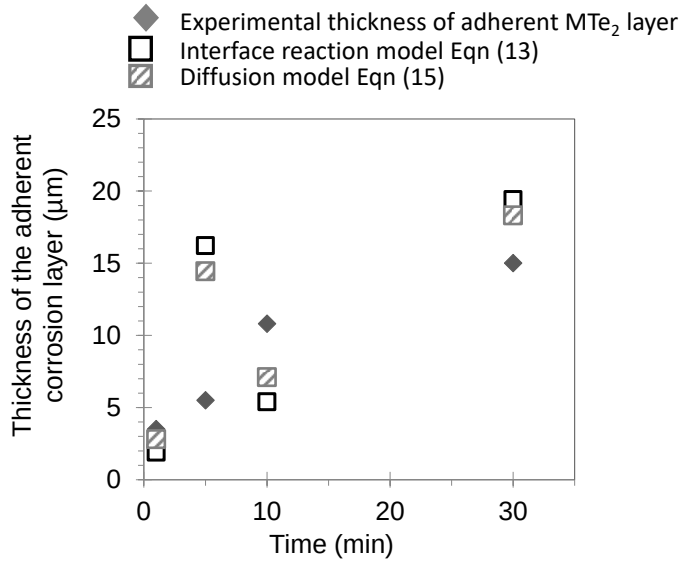

Figure 34: Scale growth kinetics: measured from SEM observation, (♦), and predicted from Equation 13 (□) and Equation 15 (▨).